OCEANOGRAPHY

Global oceanic oxygenation controlled by the Southern Ocean through the last deglaciation

Yi Wang[1,2,3]*, Kassandra M. Costa[1], Wanyi Lu[1], Sophia K. V. Hines[4], Sune G. Nielsen[1,2,5]

Ocean dissolved oxygen (DO) can provide insights on how the marine carbon cycle affects global climate change. However, the net global DO change and the controlling mechanisms remain uncertain through the last deglaciation. Here, we present a globally integrated DO reconstruction using thallium isotopes, corroborating lower global DO during the Last Glacial Maximum [19 to 23 thousand years before the present (ka B.P.)] relative to the Holocene. During the deglaciation, we reveal reoxygenation in the Heinrich Stadial 1 (~14.7 to 18 ka B.P.) and the Younger Dryas (11.7 to 12.9 ka B.P.), with deoxygenation during the Bølling-Allerød (12.9 to 14.7 ka B.P.). The deglacial DO changes were decoupled from North Atlantic Deep Water formation rates and imply that Southern Ocean ventilation controlled ocean oxygen. The coherence between global DO and atmospheric CO_2 on millennial timescales highlights the Southern Ocean's role in deglacial atmospheric CO_2 rise.

INTRODUCTION

Oceanic dissolved oxygen (DO) is supplied from air-sea exchange and photosynthesis in the photic zone, and it is consumed by organic carbon respiration throughout the water column. Because respired carbon accumulation and oxygen consumption are stoichiometrically linked during organic carbon degradation, DO reconstructions are particularly valuable for understanding marine respired carbon storage (1), which plays a major role in the glacial-interglacial variability of the partial pressure of atmospheric CO_2 (pCO_2) (1).

The most recent compilation of available DO proxy records (e.g., laminations, foraminiferal assemblages, redox-sensitive metals, bulk sedimentary nitrogen isotopes, and carbon isotopic composition records) captures this inverse relationship between marine carbon storage and DO (2–4). However, all presently available DO reconstructions are influenced by local variability in ventilation (e.g., changes in upwelling intensity) and/or export of organic matter to the sediment (5), making it challenging to determine the average global state of oceanic oxygenation. For instance, increased DO has been observed during the Bølling-Allerød [B-A; 12.9 to 14.7 thousand years before the present (ka B.P.); also known as the Antarctic Cold Reversal (ACR)] in the deep Atlantic (>2000 m) as a result of the recovery of Atlantic Meridional Overturning Circulation (AMOC) (2, 6), whereas the upper (<1500 m) Indo-Pacific experienced DO loss in the same interval (2). Spatially heterogeneous DO reconstructions thus complicate extrapolation from local to globally integrated oxygenation responses and how these relate to marine carbon storage and global climate change.

The seawater thallium isotopic composition (ε^{205}Tl, normalized ^{205}Tl/^{203}Tl in parts per 10,000) is a promising qualitative indicator of the global DO content that can record transient oxygenation responses on multi-millennial (several thousand years) timescales (7, 8). The modern seawater thallium isotopic composition is homogenous at

ε^{205}Tl = −6.0 ± 0.3 (SD) due to its long residence time (~22 ka) compared to the deep ocean overturning time (7). Because of the relatively invariant isotopic composition (ε^{205}Tl of −2) of oceanic Tl sources, seawater ε^{205}Tl is mainly modulated by the oceanic Tl sinks on glacial-interglacial timescales, primarily through oxidative sorption of Tl onto manganese oxides that preferentially removes ^{205}Tl relative to ^{203}Tl from the ocean (9, 10) (Supplementary Materials). Manganese oxide burial is directly linked to oceanic oxygenation because manganese oxides require ambient oxygen to form (7). As ocean oxygen decreases and low-oxygen waters expand, reductive dissolution of manganese oxide in the water columns and/or sediments would increase the dissolved Mn(II) reservoir in the ocean and decrease ^{205}Tl scavenged via Mn oxide burial, resulting in heavier seawater Tl isotopic compositions (higher ε^{205}Tl values) (Supplementary Materials). Seawater ε^{205}Tl variations are recorded in sediments deposited with reducing porewaters (11, 12), where complete removal of Tl from the ambient waters (likely by iron sulfides) leads to zero net isotopic fractionation (12). Oxygen minimum zone (OMZ) sediments (where reducing porewaters prevail) are therefore potential archives for past seawater Tl isotopic compositions and global oceanic oxygenation.

Here, we report the first globally integrated DO content reconstruction at high resolution (150 to 500 years) from the Last Glacial Maximum (LGM; 19 to 23 ka B.P.) to today using seawater thallium isotope reconstructions from the Arabian Sea OMZ (TN041-8PG and TN041-8JPC, 17°48.76′N, 57°30.34′E, 761-m water depth). The Arabian Sea OMZ intensity is closely linked with export productivity associated with monsoon-driven upwelling (13) and ventilation by intermediate water masses (e.g., Antarctic Intermediate Water in glacial times) (14). The cores TN041-8PG/JPC were deposited under persistent low-oxygen environments in the past ~30 ka, as evidenced by redox-sensitive trace metals and benthic foraminiferal surface porosity (fig. S1) (15). Fidelity of the authigenic sedimentary ε^{205}Tl record with contemporaneous seawater values was confirmed through the decision tree constructed from a recent global core top calibration (Materials and Methods) (12). Authigenic sedimentary ε^{205}Tl values also show decoupled changes from the local DO variations (fig. S1) (15), corroborating that the authigenic ε^{205}Tl record is not controlled by local factors (e.g., ventilation or export productivity). Our results reveal lower global DO during the LGM compared to the Holocene (0 to 11.7 ka B.P.), as well as systematic

[1]Department of Geology and Geophysics, Woods Hole Oceanographic Institution, Woods Hole, MA 02543, USA. [2]NIRVANA Laboratories, Woods Hole Oceanographic Institution, Woods Hole, MA 02543, USA. [3]Department of Earth and Environmental Sciences, Tulane University, New Orleans, LA 70118, USA. [4]Department of Marine Chemistry and Geochemistry, Woods Hole Oceanographic Institution, Woods Hole, MA 02543, USA. [5]Centre de Recherches Pétrographiques et Géochimiques, CNRS, Université de Lorraine, 15 rue Notre Dame des Pauvres, 54501 Vandoeuvre lès Nancy, France.
*Corresponding author. Email: ywang@whoi.edu, ywang145@tulane.edu

oxygenation changes in response to millennial events across the last deglaciation. Most of the global DO rise from the LGM to the Holocene occurred in the Heinrich Stadial 1 (HS1) and the Younger Dryas (YD), but a brief period of deoxygenation characterized the B-A/ACR.

RESULTS AND DISCUSSIONS

Lower global ocean oxygen content in the LGM compared to the Holocene

In the Holocene, the authigenic ε^{205}Tl values were relatively stable [ε^{205}Tl = −6.1 ± 0.4 (SD), n = 31] and indistinguishable from the modern seawater value of ε^{205}Tl = −6.0 ± 0.3 (SD), suggesting that global ocean DO has remained relatively constant through the Holocene (Fig. 1). At ~3.5 ka B.P., authigenic ε^{205}Tl values briefly decreased to ε^{205}Tl ~ −6.5, which could imply a short period of higher oceanic oxygenation. The exact cause of this higher DO interval remains to be investigated. In contrast, ε^{205}Tl values indicate persistently lower global DO content in the last glacial period (18 to 32 ka B.P.), with an average ε^{205}Tl value of −5.1 ± 0.3 (SD, n = 30). If we apply a steady-state mass balance model (Supplementary Materials), then the mean ε^{205}Tl value during the last glacial period would correspond to an 18 ± 6% (SD based on analytical uncertainty of ε^{205}Tl; Supplementary Materials) lower Mn oxide burial flux compared to the Holocene, possibly related to concurrent changes in dissolved Mn(II) of seawater. For example, lower glacial DO could have led to higher dissolved Mn(II) in the water columns, followed by reoxidation to Mn oxide under increased oceanic DO in the Holocene (1, 16). A smaller global oceanic DO reservoir during the LGM occurred despite the generally more oxygenated conditions in the upper ocean (<1500 m) at this time (Fig. 2) (2, 17). Therefore, the reduction of DO content in the deep ocean must have exceeded the DO rise in the upper ocean (2) during the LGM to drive a net decline of the global DO content, implying that the oceanic DO reservoir is primarily controlled by the deep ocean. This inference is consistent with the fact that ~63% of the ocean volume (and ~85% of the seafloor) resides in waters deeper than 1500 m (Supplementary Materials).

Our record provides the first global picture of lower oceanic DO content during the LGM relative to the Holocene, and it is consistent with previously published records of, e.g., local oxygenation reconstructions in the deep ocean (2, 3, 18), ventilation records from radiocarbon (19, 20), and intermediate-complexity model simulations (21, 22). The global DO content can be modulated by oxygen solubility (controlled by oceanic temperature), export productivity from the photic zone that consumes oxygen in subsurface waters under respiration (i.e., the soft tissue pump), and ventilation (e.g., air-sea gas exchange of upwelled waters and subsurface water formation rates). Because the global DO content is controlled by the deep ocean (Fig. 2), we focus on the forcing mechanisms that may have dominated the deep ocean oxygen variability. The observed lower DO content during the LGM is opposite to the higher oxygen solubility in seawater at lower temperatures (23), ruling solubility out as a driver of oceanic DO changes from LGM to Holocene. The contribution of LGM export productivity to lowering deep ocean oxygen remains uncertain. Higher LGM export productivity has been observed in the Subantarctic Zone associated with enhanced dust input (fig. S4) (24), which could have drawn down ocean oxygen via respiration. However, lower export productivity in LGM has

been found elsewhere (25–29). In addition, the difference between the planktic and benthic foraminifera stable carbon isotopic compositions (δ^{13}C) in the LGM was recently shown to be similar to the modern values in the deep Pacific Ocean, suggesting that respiration of export productivity alone may not fully explain the observed reduced deep ocean oxygen (30). Deep ocean ventilation is primarily controlled by the strength of deep water formation in the North Atlantic [via North Atlantic Deep Water (NADW) formation] and Southern Ocean [via Antarctica Bottom Water (AABW) formation]. With glacial NADW potentially limited to the upper 2000 m, the LGM deep ocean was primarily occupied by AABW (31, 32), which forms along the Antarctica margin following poleward transport of the upwelled NADW in the Antarctic Zone. Less ventilated AABW is thus likely needed to drive a net reduction of deep ocean DO during the LGM. Glacial AABW was more isolated due to extensive sea ice (limiting air-sea gas exchange) and weakened upwelling (22, 28, 33, 34), and such isolation also allows continued oxygen consumption in the deep ocean. In addition, the remineralization depth could have been deeper due to slower organic carbon respiration rates under cooler LGM temperatures, which could have allowed additional export carbon sinking into the deep ocean (35–37). Despite the lack of observational evidence, this mechanism may further reduce the deep ocean oxygen content even without a substantial change of export flux or ocean circulation.

Millennial global ocean oxygen variability during the deglaciation

During the deglaciation, the seawater ε^{205}Tl record reveals millennial variations of global oceanic oxygenation and Mn oxide burial in the ocean, which could have led to non–steady-state Tl isotope mass balance. The transient seawater ε^{205}Tl changes can be simulated using a non–steady-state box model by perturbing Mn oxide fluxes (Supplementary Materials and fig. S5). Rapid deoxygenation in the global ocean in the B-A/ACR (Fig. 1) may have led to enhanced reductive dissolution of Mn oxides and Mn(II) supply from organic carbon respiration (38). An increased global deep ocean oxygen content relative to the LGM is evidenced by shifts toward more negative seawater ε^{205}Tl values during the cold intervals in the Northern Hemisphere (HS1 and YD), which could have also triggered excessive Mn oxide burial fluxes due to an elevated Mn(II) reservoir in the low-oxygen LGM and B-A/ACR, respectively (Supplementary Materials). These distinct intervals of deep ocean DO changes are likely not related to temperature-driven solubility [as mean ocean temperature closely follows atmospheric pCO_2; (23) and fig. S1] or export productivity in the Antarctic Zone (Fig. 1) (28). As the subantarctic-sourced water primarily ventilates the upper ocean [<2000-m water depth; (39)], reduced export productivity (under declined dust input) and less complete nutrient consumption compared to the LGM (24, 40) also suggest that the Subantarctic Zone may not be a major contributor to the deep ocean oxygen content (fig. S4).

Deep ocean ventilation changes via NADW and/or AABW formation likely served as the primary driver of the observed deglacial DO variability. Strengthened NADW formation that supplied oxygen-rich surface water to the deep ocean resulted in a better ventilated deep Atlantic (2, 19, 41) and, possibly, Indian Ocean (42) during the B-A/ACR (Fig. 1E). A more oxygenated Atlantic, however, contrasts with our reconstructed global ocean oxygen content at the
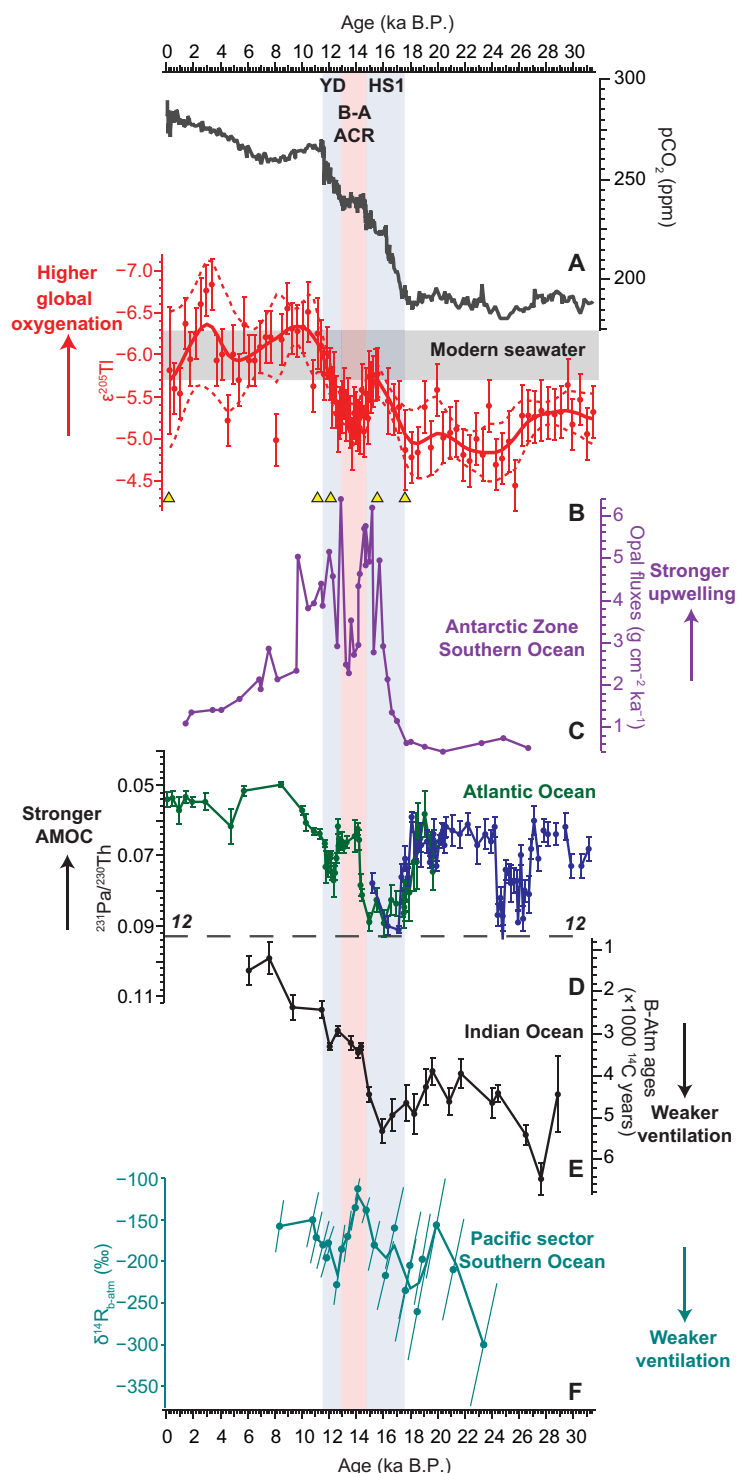
Fig. 1. Global oceanic oxygenation reconstructions compared with global climate and ocean circulation records. (**A**) Atmospheric CO_2 concentrations from the Antarctic composite ice core records (54). ppm, parts per million. (**B**) authigenic sedimentary $\varepsilon^{205}Tl$ record from the core TN041-8PG/8JPC with the LOESS fit (Materials and Methods) shown in the solid red curve and the bootstrapped 2-SD envelope shown in the dashed red curve. Error bars are in 2 SD. When the measurement 2 SD is smaller than 0.3, the error bar was set to 0.3 (the long-term reproducibility of $\varepsilon^{205}Tl$ analyses, see Materials and Methods). ^{14}C dates were shown in the yellow triangles. (**C**) Opal fluxes of TN057-13PC as an upwelling proxy in the Southern Ocean (28). (**D**) $^{231}Pa/^{230}Th$ activity ratios from the Bermuda Rise as an indicator of AMOC strength from the core OCE326 GGC-5 (green) (43) and ODP Site 1063 (blue) (44). The error bar represents 2 SE. The production ratio of $^{231}Pa/^{230}Th$ in the water columns is shown in the horizontal dashed line. (**E**) Radiocarbon age offsets between benthic foraminifera and the atmosphere (B-Atm) as a proxy for subsurface water mass ventilation from the Indian Ocean core SS172/4040 (42). The error bar is 2 SD. (**F**) The relative deviation ($\delta^{14}R$) between the deep water and the atmospheric $\Delta^{14}C$ as an indicator for deep water ventilation from the Pacific Ocean at core MD97-2106 (47). Error bars are 1 SD. The HS1 and YD are shaded in light blue, whereas B-A/ACR is shaded in light red.
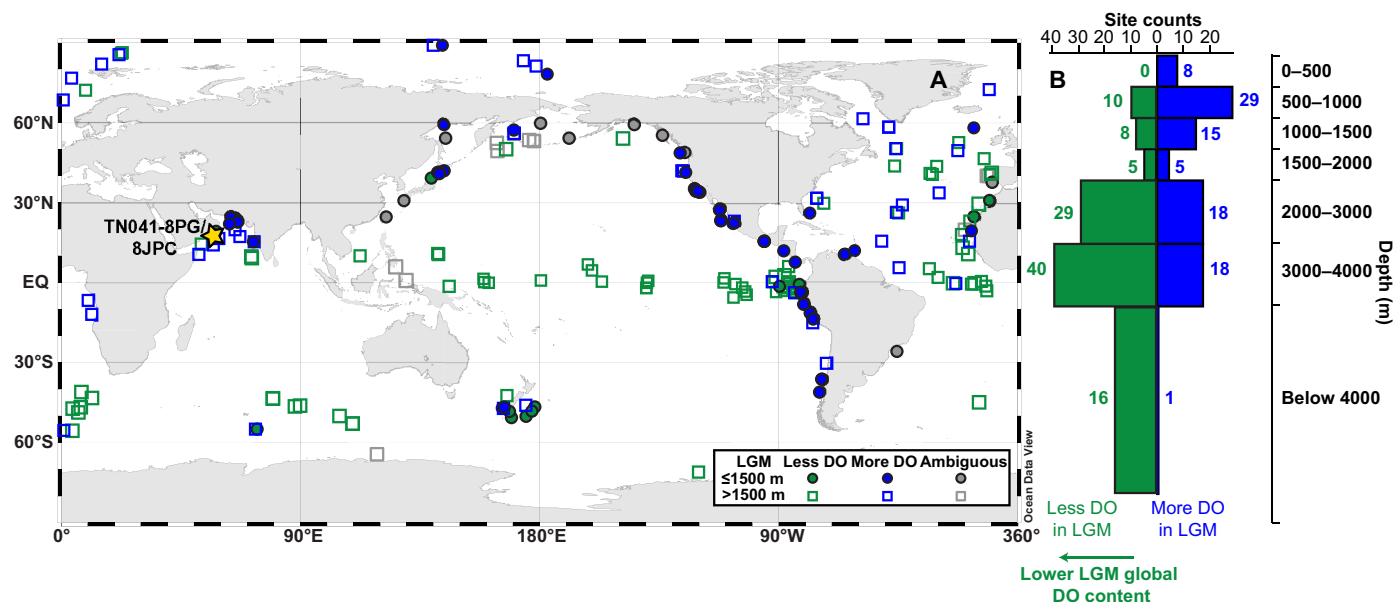
Fig. 2. Compilation of qualitative oxygenation changes between the LGM and the Holocene from localized redox proxies. (**A**) The upper ocean sites (water depth ≤ 1500 m) are denoted by solid circles, whereas the deep ocean sites (water depth > 1500 m) are represented by hollow squares. Lower, higher, and ambiguous changes in bottom water oxygenation during LGM compared to the Holocene are shown in green, blue, and gray symbols, respectively. Whenever there is an overlap, blue overlies green, which overlies the gray symbols. The studied site (TN041-8PG/8JPC) is shown in the yellow star. Base map was generated using Ocean Data View (75). (**B**) The number of compiled sites that show lower and higher oxygenation in LGM relative to the Holocene binned by the water depth. The bottom green arrow shows the globally integrated oceanic DO content change indicated by reconstructed seawater thallium isotopic composition change.

same time. We note that global DO variability from Tl isotopes through the deglaciation is anti-phased with NADW formation rates (Fig. 1) reconstructed from $^{231}Pa/^{230}Th$ (43–45), arguing against an NADW ventilation control on the global deep ocean oxygenation. Despite recent studies debating whether NADW formation completely halted during the HS1 (46), a consensus remains that NADW formation was weaker during the deglacial stadial periods relative to interstadial periods. Because our data do not align with that framework, they instead point to AABW ventilation as the most probable means of modulating the global DO content during the deglaciation. This conclusion is consistent with a radiocarbon reconstruction in the deep southwest Pacific, which shows development of poorly ventilated water masses starting from the early B-A/ACR but increasingly ventilated conditions in the HS1 and YD (Fig. 1F) (47). Redox-sensitive trace metal (e.g., authigenic uranium and manganese) records from Atlantic sectors of the deep Southern Ocean also show similar oxygenation in YD and HS1 (1).

Deep Southern Ocean ventilation is likely related to migration and strength of Southern Hemisphere westerlies (48, 49). For example, southward displacement and intensification of westerlies during HS1 and YD would have increased upwelling and abyssal mixing in the Southern Ocean (50), leading to a less stratified water column and new AABW formation (48). A southward displacement of the westerlies would also have contributed to Antarctic Zone warming via southward eddy heat transport (49, 51). Subsequent reduction of Antarctica sea ice cover would have promoted air-sea gas exchange (52) and additional AABW ventilation (53). Conversely, during the B-A or ACR, expanded sea ice and northward migration of westerlies would have triggered the opposite oceanic DO response.

Coherence between reconstructed global ocean oxygen and atmospheric CO₂

The high-resolution $\varepsilon^{205}Tl$ reconstruction of the global DO content also shows notable coherence with atmospheric CO_2 concentrations (Supplementary Materials and Figs. 1 and 3; $r = -0.74$, $P < 0.01$), corroborating the ocean's role in modulating pCO_2 variability throughout the last glacial period (at least to 32 ka B.P.). A smaller oceanic DO reservoir in the LGM suggested by the less negative $\varepsilon^{205}Tl$ values corresponds to lower pCO_2, whereas deglacial $\varepsilon^{205}Tl$ variability on millennial timescales displays nearly synchronous variability with the two-step pCO_2 rise (54). Transitions toward a higher global DO content correspond to pCO_2 increase during 15.5 to 17.5 ka B.P. (HS1) and 12.9 to 11.7 ka B.P. (YD), whereas the pCO_2 plateau during B-A/ACR was contemporaneous with the lowest global DO content in the deglaciation, suggesting a pause in CO_2 release from the ocean (55). The Southern Ocean control on the global DO reservoir would then imply that CO_2 outgassing from the Southern Ocean rather than the Atlantic Ocean likely dominated the oceanic contribution to the deglacial pCO_2 changes. As NADW formation recovered following the HS1 and the deep Atlantic became more ventilated in the B-A/ACR, a Southern Ocean control on deglacial ocean oxygenation thus also provides a plausible explanation for stagnant atmospheric pCO_2 at this time (19). However, NADW formation may still play an important role in regulating ocean carbon storage. For instance, NADW formation during LGM could have transported CO_2 into the deep ocean through entrainment into AABW (56). During the last deglaciation, abrupt changes of NADW formation rates may have triggered more rapid changes (e.g., sub-millennial) in atmospheric pCO_2 that cannot be resolved in our record (57, 58). We also caution that our global ocean oxygen reconstruction cannot constrain other controls of ocean carbon storage (e.g., carbonate pump
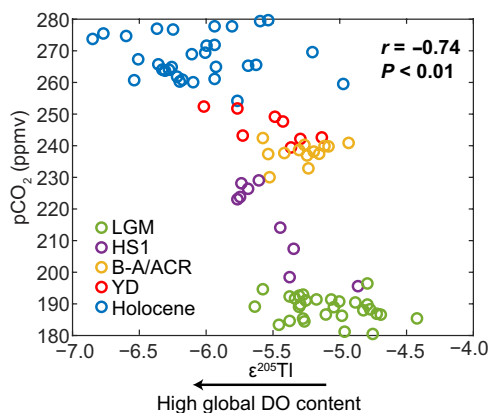
Fig. 3. Pearson correlation between atmospheric pCO2 and authigenic Tl isotopic compositions. The atmospheric pCO2 data are from (*54*). The Pearson correlation is statistically significant (*P* < 0.01). The LGM, HS1, B-A/ACR, YD, and the Holocene are denoted by green, purple, yellow, red, and blue circles, respectively.

and air-sea gas disequilibrium) that could have contributed to the deglacial pCO_2 change synergistically.

Implications for future ocean oxygenation

Predicting future oceanic oxygenation under anthropogenic climate change remains challenging, but sedimentary archives may provide insights for future model development on how physical (e.g., ocean mixing and sea ice formation) and biogeochemical processes (e.g., productivity and respiration) will respond. Observations and model simulations suggest poleward migration and intensification of southern westerlies in recent decades and, possibly, in the future, which may lead to a more ventilated Southern Ocean (*50*, *59*). However, observed freshening of AABW since the 1990s due to Antarctic meltwater could reduce deep ocean oxygenation (*30*, *60*). Whether the deep Southern Ocean will become more oxygenated in response to the ongoing climate change is thus still under debate. Our reconstruction on the globally integrated ocean oxygen variability would then be consistent with recent model predictions implying a more ventilated Southern Ocean on centennial to millennial timescales under future warming (*61*), which may lead to higher global deep ocean oxygen content as ventilation outpaces ocean warming and stratification.

MATERIALS AND METHODS
Materials and age models
The cores TN041-8PG/8JPC (17°48.76′N, 57°30.34′E, 761-m water depth) were retrieved from the Oman margin through the US Joint Global Ocean Flux Study Arabian Sea Process Study. The intermediate waters that affect the Arabian Sea OMZ include the saline Red Sea Intermediate Water, Persian Gulf Water, and the southern-sourced Indian Central Water produced by mixing of aged Antarctic Intermediate Water (AAIW) and Indonesian Intermediate Water (*62*). Persian Gulf Water and Red Sea Intermediate Water are relatively oxygenated due to recent contact with the atmosphere before being exported into the Arabian Sea (*63*). The Indian Central Water, however, is nutrient-rich and low-DO due to oxygen consumption by organic carbon respiration in AAIW on its path to the Arabian Sea (*62*). During glacial times with low sea level, water exchange

between the Red Sea and Arabian Sea could be greatly reduced, with a stronger AAIW ventilation in the Arabian Sea (*14*). Previous research has shown coeval responses of stronger AAIW ventilation in the Arabian Sea and the North Atlantic Heinrich events that weakened the thermohaline circulation (*14*). Bulk sediment samples were taken from the cores at a 4-cm resolution (~150 to 500 years, a total of 90 samples) and were freeze dried. The age model was taken from (*15*). Briefly, ages were estimated using the $\delta^{18}O$ stratigraphy of *Globigerinoides ruber* first, and, then, seven accelerator mass spectrometry ^{14}C dates were generated from an average of 300 to 350 individuals of *G. ruber* picked from the >250- or > 335-μm-size fractions, at the National Ocean Sciences Accelerator Mass Spectrometry Facility at Woods Hole Oceanographic Institution (WHOI). Planktic ^{14}C dates were converted into calendar ages using the Marine20 curve (*64*) with an Arabian Sea regional marine radiocarbon reservoir age correction $\Delta R = 93 \pm 61$ years (*65*), using Bacon (rbacon package) that uses adaptive Markov chain Monte Carlo algorithm and Bayesian statistics (*66*).

Bulk elemental concentrations and enrichment factors
A fraction of freeze-dried sediments was ground into powder using an agate mortar and pestle for bulk elemental concentration and thallium isotope analyses. Sedimentary U and Al have been published by (*15*). Here, we summarize the bulk elemental concentration method. Samples were selected at a 16-cm resolution through the core. About 10 mg of bulk freeze-dried samples was digested using a mixture of 1 ml of concentrated nitric acid (HNO_3), 1 ml of hydrofluoric acid (HF), and 0.1 ml of hydrochloric acid (HCl) at 135°C. Aqua regia (3:1 mixture of HCl and HNO_3) was used to remove fluoride precipitates formed during the HF digestion. The dried sample was redissolved in 2% HNO_3 and diluted for analyses on the Thermo iCAP Q inductively coupled plasma mass spectrometer (ICP-MS) at WHOI. Two standard calibration curves were used, including rock [BHVO-2 (basalt) and AGV-2 (andesite), US Geological Survey] and high-purity ICP-MS elemental standards. Indium was used as an internal standard to monitor the instrument drift. MESS-3 (continental margin sediments, National Research Council of Canada) was used as the standard reference material to monitor accuracy, which yielded an external recovery of 96 to 113% for all certified elements. Long-term reproducibility of the elemental concentrations was monitored by the relative SD of repeated measurements of the MESS-3 digested with each batch of samples, which was <10%.

Authigenic Tl isotopic composition measurements
Thallium isotopic compositions [$\epsilon^{205}Tl = 10{,}000 \times (^{205}Tl/^{203}Tl_{sample} - ^{205}Tl/^{203}Tl_{NIST\ SRM997})/(^{205}Tl/^{203}Tl_{NIST\ SRM997})$] were determined for the authigenic component of the sediments. The authigenic component was extracted by immersion of approximately 100 mg of ground bulk sediments in 2 M nitric acid at 130°C for 12 to 15 hours, primarily targeting Fe sulfides (main host phase of Tl in the reducing environments) with minimal impacts from the detrital fraction (*11*, *12*, *67*). Authigenic fractions were then separated by pipetting out the supernatant following centrifugation. The supernatant was dried down and repeatedly digested with inverse aqua regia (1:3 mixture of HCl and HNO_3) and hydrogen peroxide (H_2O_2) at 130°C to remove organic matter. Last, samples were dissolved in 1 ml of 1 M HCl, and 30 μl of brominated water (Br_2-H_2O) was added to oxidize Tl(I) to Tl(III) for column chemistry (*68*). The standard reference material SCo-1 (Cody shale, US Geological

Survey) was also processed in the same manner to monitor sample reproducibility. One mini-column with 100-μl anion exchange resin (AG 1-X8) was used to achieve efficient Tl separation following the well-established procedures (67–69). The resin was cleaned and precondtioned with 1.5 ml of 0.1 M HCl–5% SO_2, 1.5 ml of 0.1 M HCl, and $0.1 + 0.3 \times 3$ ml of 0.1 M HCl–1% Br_2-H_2O. Digested samples in 1 M HCl–3% Br_2-H_2O were loaded onto the columns, followed by the addition of $0.1 \times 3 + 1.5$ ml of solutions of 0.5 M HNO_3–3% Br_2-H_2O, $0.1 + 1.5$ ml of 2 M HNO_3–3% Br_2-H_2O, and 0.1 ml of 0.1 M HCl–1% Br_2-H_2O to elute the sample matrix. Thallium was then eluted with $0.1 + 1.5$ ml of 0.1 M HCl–5% SO_2 solution. The collected solution was then dried down and dissolved in 0.5 ml of 0.1 M $HNO_3 + 0.1\%$ H_2SO_4 solution. All Tl isotope analyses were performed on a Thermo Finnigan Neptune multi-collector ICP-MS at the WHOI Plasma Facility, using standard-sample bracketing and external normalization to Pb (68). Each sample were measured at least twice for ε^{205}Tl and a long-term external reproducibility of $\sim \pm 0.30$ ε^{205}Tl units (2 SD) (11, 70). SCo-1 standard measurements yielded a Tl isotopic composition of -2.83 ± 0.10 (SD, $n = 2$), which is identical to previously published values (7).

Authigenic sedimentary ε^{205}Tl for the cores TN041-8PG/8JPC

Recent work has shown that quantitative Tl removal by sulfides can occur in the ambient sediment porewaters under manganous (no oxygen with Mn reduction) conditions (71). If quantitative Tl removal occurs at/near the sediment interface, then authigenic sedimentary ε^{205}Tl faithfully preserves the overlying seawater ε^{205}Tl value (12). A decision tree based on modern sediment core top data has recently been developed to test fidelity of sediment archives in preserving the seawater ε^{205}Tl value (12), where Mn, U, and Ba enrichment factors (Mn_{EF}, U_{EF}, and Ba_{EF}) with respect to the upper continental crust (72) are used as input variables. The elemental enrichment factors of the core TN041-8PG/8JPC are calculated using the following equation

$$\text{Element}_{EF} = \frac{\left(\frac{\text{Element}}{\text{Al}} \right)_{\text{sample}}}{\left(\frac{\text{Element}}{\text{Al}} \right)_{\text{UCC}}}$$

The calculated Mn_{EF}, U_{EF}, and Ba_{EF} (table S2) were passed through the decision tree and yielded 100% positive output, which implies that the sedimentary ε^{205}Tl values measured in our cores record the overlying water column value. Despite the lower U_{EF} values during the LGM that indicates better oxygenated conditions [~10 to 15 μmol/kg higher; (15) and fig. S1], positive output from the decision tree implies that porewaters at/near the sediment-water interface were still sufficiently reducing for quantitative Tl removal. The persistent low-oxygen condition through the last LGM is also consistent with foraminiferal I/Ca reconstructions from the same core, which indicate that both LGM and Holocene local bottom water oxygen was <50 μmol/kg (15).

Postdepositional Mn remobilization is unlikely to affect authigenic ε^{205}Tl in the studied core. If Mn oxide preservation had occurred at/near the sediment-water interface due to higher bottom water oxygen during the LGM, then preferential uptake of ^{205}Tl upon sorption onto Mn oxides would have led to much heavier sedimentary ε^{205}Tl [>−2, the marine Tl input value (7)] as has been observed in the Toarcian Peniche section (73). However, persistent U enrichment throughout the cores (fig. S1) suggests that porewaters were always reducing through the LGM and argues against preservation of Mn oxides at any time. Therefore, we conclude that

the authigenic sedimentary ε^{205}Tl should reflect the open ocean seawater throughout the record.

Statistical analyses of authigenic ε^{205}Tl

The mean and SD values of authigenic sedimentary ε^{205}Tl during LGM and the Holocene were obtained by bootstrapping the datasets 10,000 times in MATLAB. The LGM period in the core based on ε^{205}Tl variations (18 to 32 ka B.P., before the HS1) was compared with the Holocene (0 to 11.7 ka B.P., after the YD) ε^{205}Tl values. The two intervals show statistical mean values that are significantly different (fig. S2). The presented authigenic ε^{205}Tl record has also been smoothed by a nonparametric regression [locally estimated scatterplot smoothing (LOESS) function]. The robust LOESS algorithm was used, which performs local regressions with weighted linear least squares and a second-degree polynomial model that assigns lower weights on the outliers. The span (i.e., fraction of the data points used for local regression) of LOESS fit was optimized using cross-validation (74). A total of 99 fractions (1 to 99% of the data used for LOESS regression) were tested to minimize the final residual error of the LOESS fit. For each fraction, the cross-validation process divided the original dataset into 10 splits, with each realization using 9 splits as the training data for obtaining the LOESS fit and the remaining 1 split as the test data to determine the residual. The optimized fraction was selected on the basis of the smallest cross-validated residual, which yielded a span of 14%. The best LOESS fit curve and the 2-SD confidence intervals were then obtained through 10,000 realizations generated by the bootstrapping approach.

To determine the correlation between atmospheric pCO_2 (54) and authigenic Tl isotopic composition over the past 32,000 years, the much higher resolution ice core pCO_2 composite record was first interpolated onto the ages of authigenic ε^{205}Tl record for comparison. A Pearson correlation coefficient was then computed between the interpolated pCO_2 and the LOESS fit of authigenic ε^{205}Tl, and a P value was used to determine the significance (Fig. 3). Cross-correlation of the two time series was also determined after adding 400-year time lags to one of the records (median temporal resolution in the authigenic Tl isotopic composition record) in MATLAB (fig. S3). These analyses reveal that the statistically most significant correlation between pCO_2 and ε^{205}Tl is observed when no time lag between the two time series is applied. Such strong correlation also suggests that pCO_2 changes during the last deglaciation were closely linked with ocean ventilation that simultaneously also exerted control over the global ocean oxygen budget.

Supplementary Materials

This PDF file includes:
Supplementary Text
Figs. S1 to S5
Legends for tables S1 and S2
Table S3
References

Other Supplementary Material for this manuscript includes the following:
Tables S1 and S2

REFERENCES AND NOTES

1. S. L. Jaccard, E. D. Galbraith, A. Martínez-Garciá, R. F. Anderson, Covariation of deep Southern Ocean oxygenation and atmospheric CO₂ through the last ice age. *Nature* **530**, 207–210 (2016).
2. S. L. Jaccard, E. D. Galbraith, Large climate-driven changes of oceanic oxygen concentrations during the last deglaciation. *Nat. Geosci.* **5**, 151–156 (2012).
3. A. W. Jacobel, R. F. Anderson, S. L. Jaccard, J. F. McManus, F. J. Pavia, G. Winckler, Deep Pacific storage of respired carbon during the last ice age: Perspectives from bottom water oxygen reconstructions. *Quat. Sci. Rev.* **230**, 106065 (2020).

4. Y. Zhou, J. F. McManus, Authigenic uranium deposition in the glacial North Atlantic: Implications for changes in oxygenation, carbon storage, and deep water-mass geometry. *Quat. Sci. Rev.* **300**, 107914 (2023).

5. C. Deutsch, H. Brix, T. Ito, H. Frenzel, L. A. Thompson, Climate-forced variability of ocean hypoxia. *Science* **333**, 336–339 (2011).

6. E. D. Galbraith, S. L. Jaccard, Deglacial weakening of the oceanic soft tissue pump: Global constraints from sedimentary nitrogen isotopes and oxygenation proxies. *Quat. Sci. Rev.* **109**, 38–48 (2015).

7. S. G. Nielsen, M. Rehkämper, J. Prytulak, Investigation and application of thallium isotope fractionation. *Rev. Mineral. Geochem.* **82**, 759–798 (2017).

8. Y. Wang, S. Bodin, J. S. Blusztajn, C. Ullmann, S. G. Nielsen, Orbitally paced global oceanic deoxygenation decoupled from volcanic CO_2 emission during the middle Cretaceous Oceanic Anoxic Event 1b (Aptian-Albian transition). *Geology* **50**, 1324–1328 (2022).

9. S. G. Nielsen, L. E. Wasylenki, M. Rehkämper, C. L. Peacock, Z. Xue, E. M. Moon, Towards an understanding of thallium isotope fractionation during adsorption to manganese oxides. *Geochim. Cosmochim. Acta* **117**, 252–265 (2013).

10. C. L. Peacock, E. M. Moon, Oxidative scavenging of thallium by birnessite: Explanation for thallium enrichment and stable isotope fractionation in marine ferromanganese precipitates. *Geochim. Cosmochim. Acta* **84**, 297–313 (2012).

11. J. D. Owens, S. G. Nielsen, T. J. Horner, C. M. Ostrander, L. C. Peterson, Thallium-isotopic compositions of euxinic sediments as a proxy for global manganese-oxide burial. *Geochim. Cosmochim. Acta* **213**, 291–307 (2017).

12. Y. Wang, W. Lu, K. M. Costa, S. G. Nielsen, Beyond anoxia: Exploring sedimentary thallium isotopes in paleo-redox reconstructions from a new core top collection. *Geochim. Cosmochim. Acta* **333**, 347–361 (2022).

13. G. J. Reichart, S. J. Schenau, G. J. De Lange, W. J. Zachariasse, Synchroneity of oxygen minimum zone intensity on the Oman and Pakistan Margins at sub-Milankovitch time scales. *Mar. Geol.* **185**, 403–415 (2002).

14. S. J. A. Jung, D. Kroon, G. Ganssen, F. Peeters, R. Ganeshram, Enhanced Arabian Sea intermediate water flow during glacial North Atlantic cold phases. *Earth Planet. Sci. Lett.* **280**, 220–228 (2009).

15. W. Lu, Y. Wang, D. W. Oppo, S. G. Nielsen, K. M. Costa, Comparing paleo-oxygenation proxies (benthic foraminiferal surface porosity, I/Ca, authigenic uranium) on modern sediments and the glacial Arabian Sea. *Geochim. Cosmochim. Acta* **331**, 69–85 (2022).

16. A. Mangini, A. Eisenhauer, P. Walter, Response of manganese in the ocean to the climatic cycles in the Quaternary. *Paleoceanogr. Paleoclimatol.* **5**, 811–821 (1990).

17. E. D. Galbraith, M. Kienast, T. F. Pedersen, S. E. Calvert, Glacial-interglacial modulation of the marine nitrogen cycle by high-latitude O_2 supply to the global thermocline. *Paleoceanogr. Paleoclimatol.* **19**, 1–12 (2004).

18. B. A. A. Hoogakker, H. Elderfield, G. Schmiedl, I. N. McCave, R. E. M. Rickaby, Glacial–interglacial changes in bottom-water oxygen content on the Portuguese margin. *Nat. Geosci.* **8**, 40–43 (2015).

19. L. C. Skinner, E. Freeman, D. Hodell, C. Waelbroeck, N. Vazquez Riveiros, A. E. Scrivner, Atlantic ocean ventilation changes across the last deglaciation and their carbon cycle implications. *Paleoceanogr. Paleoclimatol.* **36**, e2020PA004074 (2021).

20. E. L. Sikes, C. R. Samson, T. P. Guilderson, W. R. Howard, Old radiocarbon ages in the southwest Pacific Ocean during the last glacial period and deglaciation. *Nature* **405**, 555–559 (2000).

21. L. Menviel, J. Yu, F. Joos, A. Mouchet, K. J. Meissner, M. H. England, Poorly ventilated deep ocean at the last glacial maximum inferred from carbon isotopes: A data-model comparison study. *Paleoceanography* **32**, 2–17 (2017).

22. E. Cliff, S. Khatiwala, A. Schmittner, Glacial deep ocean deoxygenation driven by biologically mediated air–sea disequilibrium. *Nat. Geosci.* **14**, 43–50 (2021).

23. B. Bereiter, S. Shackleton, D. Baggenstos, K. Kawamura, J. Severinghaus, Mean global ocean temperatures during the last glacial transition. *Nature* **553**, 39–44 (2018).

24. A. Martínez-García, D. M. Sigman, H. Ren, R. F. Anderson, M. Straub, D. A. Hodell, S. L. Jaccard, T. I. Eglinton, G. H. Haug, Iron fertilization of the subantarctic ocean during the last ice age. *Science* **343**, 1347–1350 (2014).

25. K. M. Costa, J. F. McManus, R. F. Anderson, H. Ren, D. M. Sigman, G. Winckler, M. Q. Fleisher, F. Marcantonio, A. C. Ravelo, No iron fertilization in the equatorial Pacific Ocean during the last ice age. *Nature* **529**, 519–522 (2016).

26. G. Winckler, R. F. Anderson, S. L. Jaccard, F. Marcantonio, Ocean dynamics, not dust, have controlled equatorial Pacific productivity over the past 500,000 years. *Proc. Natl. Acad. Sci. U. S. A.* **113**, 6119–6124 (2016).

27. S. L. Jaccard, E. D. Galbraith, D. M. Sigman, G. H. Haug, A pervasive link between Antarctic ice core and subarctic Pacific sediment records over the past 800kyrs. *Quat. Sci. Rev.* **29**, 206–212 (2010).

28. R. F. Anderson, S. Ali, L. I. Bradtmiller, S. H. H. Nielsen, M. Q. Fleisher, B. E. Anderson, L. H. Burckle, Wind-driven upwelling in the southern ocean and the deglacial rise in atmospheric CO_2. *Science* **323**, 1443–1448 (2009).

29. O. Cartapanis, D. Bianchi, S. L. Jaccard, E. D. Galbraith, Global pulses of organic carbon burial in deep-sea sediments during glacial maxima. *Nat. Commun.* **7**, 10796 (2016).

30. L. D. Stott, J. Shao, J. Yu, K. M. Harazin, Evaluating the glacial-deglacial carbon respiration and ventilation change hypothesis as a mechanism for changing atmospheric CO_2. *Geophys. Res. Lett.* **48**, e2020GL091296 (2021).

31. G. Gebbie, How much did Glacial North Atlantic Water shoal? *Paleoceanography* **29**, 190–209 (2014).

32. D. W. Oppo, G. Gebbie, K. F. Huang, W. B. Curry, T. M. Marchitto, K. R. Pietro, Data constraints on glacial atlantic water mass geometry and properties. *Paleoceanogr. Paleoclimatol.* **33**, 1013–1034 (2018).

33. L. C. Skinner, S. Fallon, C. Waelbroeck, E. Michel, S. Barker, Ventilation of the deep southern ocean and deglacial CO_2 rise. *Science* **328**, 1147–1151 (2010).

34. B. B. Stephens, R. F. Keeling, The influence of antarctic sea ice on glacial-interglacial CO_2 variations. *Nature* **404**, 171–174 (2000).

35. K. Matsumoto, T. Hashioka, Y. Yamanaka, Effect of temperature-dependent organic carbon decay on atmospheric pCO_2. *J. Geophys. Res. Biogeosci.* **112**, G02007 (2007).

36. R. Roth, S. P. Ritz, F. Joos, Burial-nutrient feedbacks amplify the sensitivity of atmospheric carbon dioxide to changes in organic matter remineralisation. *Earth Syst. Dyn.* **5**, 321–343 (2014).

37. L. Menviel, F. Joos, S. P. Ritz, Simulating atmospheric CO_2, ^{13}C and the marine carbon cycle during the Last Glacial-Interglacial cycle: Possible role for a deepening of the mean remineralization depth and an increase in the oceanic nutrient inventory. *Quat. Sci. Rev.* **56**, 46–68 (2012).

38. G. P. Klinkhammer, M. L. Bender, The distribution of manganese in the Pacific Ocean. *Earth Planet. Sci. Lett.* **46**, 361–384 (1980).

39. G. Gebbie, P. Huybers, Total matrix intercomparison: A method for determining the geometry of water-mass pathways. *J. Phys. Oceanogr.* **40**, 1710–1728 (2010).

40. X. T. Wang, D. M. Sigman, M. G. Prokopenko, J. F. Adkins, L. F. Robinson, S. K. Hines, J. Chai, A. S. Studer, A. Martínez-García, T. Chen, G. H. Haug, Deep-sea coral evidence for lower Southern Ocean surface nitrate concentrations during the last ice age. *Proc. Natl. Acad. Sci. U. S. A.* **114**, 3352–3357 (2017).

41. L. C. Skinner, A. E. Scrivner, D. Vance, S. Barker, S. Fallon, C. Waelbroeck, North atlantic versus southern ocean contributions to a deglacial surge in deep ocean ventilation. *Geology* **41**, 667–670 (2013).

42. N. Bharti, R. Bhushan, L. Skinner, M. Muruganantham, P. S. Jena, A. Dabhi, A. Shivam, Evidence of poorly ventilated deep Central Indian Ocean during the last glaciation. *Earth Planet. Sci. Lett.* **582**, 117438 (2022).

43. J. F. McManus, R. Francois, J.-M. Gherardi, L. D. Keigwin, S. Brown-Leger, Collapse and rapid resumption of Atlantic meridional circulation linked to deglacial climate changes. *Nature* **428**, 834–837 (2004).

44. J. Lippold, J. Grützner, D. Winter, Y. Lahaye, A. Mangini, M. Christi, Does sedimentary $^{231}Pa/^{230}Th$ from the Bermuda rise monitor past Atlantic meridional overturning circulation? *Geophys. Res. Lett.* **36**, L12601 (2009).

45. H. C. Ng, L. F. Robinson, J. F. McManus, K. J. Mohamed, A. W. Jacobel, R. F. Ivanovic, L. J. Gregoire, T. Chen, Coherent deglacial changes in western Atlantic ocean circulation. *Nat. Commun.* **9**, 2947 (2018).

46. F. Pöppelmeier, A. Jeltsch-Thömmes, J. Lippold, F. Joos, T. F. Stocker, Multi-proxy constraints on Atlantic circulation dynamics since the last ice age. *Nat. Geosci.* **16**, 349–356 (2023).

47. Y. Dai, J. Yu, P. A. Rafter, Deglacial ventilation changes in the deep southwest pacific. *Paleoceanogr. Paleoclimatol.* **36**, e2020PA004172 (2021).

48. D. M. Sigman, F. Fripiat, A. S. Studer, P. C. Kemeny, A. Martínez-García, M. P. Hain, X. Ai, X. Wang, H. Ren, G. H. Haug, The Southern Ocean during the ice ages: A review of the Antarctic surface isolation hypothesis, with comparison to the North Pacific. *Quat. Sci. Rev.* **254**, 106732 (2021).

49. G. H. Denton, R. F. Anderson, J. R. Toggweiler, R. L. Edwards, J. M. Schaefer, A. E. Putnam, The last glacial termination. *Science* **328**, 1652–1656 (2010).

50. J. R. Toggweiler, J. L. Russell, S. R. Carson, Midlatitude westerlies, atmospheric CO_2, and climate change during the ice ages. *Paleoceanography* **21**, PA2005 (2006).

51. A. M. C. Hogg, M. P. Meredith, J. R. Blundel, C. Wilson, Eddy heat flux in the Southern ocean: Response to variable wind forcing. *J. Clim.* **21**, 608–620 (2008).

52. R. Ferrari, M. F. Jansen, J. F. Adkins, A. Burke, A. L. Stewart, A. F. Thompson, Antarctic sea ice control on ocean circulation in present and glacial climates. *Proc. Natl. Acad. Sci. U. S. A.* **111**, 8753–8758 (2014).

53. A. Schmittner, E. D. Galbraith, Glacial greenhouse-gas fluctuations controlled by ocean circulation changes. *Nature* **456**, 373–376 (2008).

54. B. Bereiter, S. Eggleston, J. Schmitt, C. Nehrbass-Ahles, T. F. Stocker, H. Fischer, S. Kipfstuhl, J. Chappellaz, Revision of the EPICA Dome C CO_2 record from 800 to 600 kyr before present. *Geophys. Res. Lett.* **42**, 542–549 (2015).

55. L. Menviel, P. Spence, J. Yu, M. A. Chamberlain, R. J. Matear, K. J. Meissner, M. H. England, Southern Hemisphere westerlies as a driver of the early deglacial atmospheric CO_2 rise. *Nat. Commun.* **9**, 2503 (2018).

56. J. Yu, L. Menviel, Z. D. Jin, D. J. R. Thornalley, G. L. Foster, E. J. Rohling, I. N. McCave, J. F. McManus, Y. Dai, H. Ren, F. He, F. Zhang, P. J. Chen, A. P. Roberts, More efficient North Atlantic carbon pump during the Last Glacial Maximum. *Nat. Commun.* **10**, 2170 (2019).

57. I. Marinov, A. Gnanadesikan, J. L. Sarmiento, J. R. Toggweiler, M. Follows, B. K. Mignone, Impact of oceanic circulation on biological carbon storage in the ocean and atmospheric pCO$_2$. *Global Biogeochem. Cycles* **22**, GB3007 (2008).

58. T. Chen, L. F. Robinson, A. Burke, J. Southon, P. Spooner, P. J. Morris, H. C. Ng, Synchronous centennial abrupt events in the ocean and atmosphere during the last deglaciation. *Science* **349**, 1537–1541 (2015).

59. R. Goyal, A. S. Gupta, M. Jucker, M. H. England, Historical and projected changes in the Southern hemisphere surface Westerlies. *Geophys. Res. Lett.* **48**, e2020GL090849 (2021).

60. K. L. Gunn, S. R. Rintoul, M. H. England, M. M. Bowen, Recent reduced abyssal overturning and ventilation in the Australian Antarctic Basin. *Nat. Clim. Chang.* **13**, 537–544 (2023).

61. T. L. Frölicher, M. T. Aschwanden, N. Gruber, S. L. Jaccard, J. P. Dunne, D. Paynter, Contrasting upper and deep ocean oxygen response to protracted global warming. *Global Biogeochem. Cycles* **34**, e2020GB006601 (2020).

62. Y. You, Intermediate water circulation and ventilation of the Indian Ocean derived from water-mass contributions. *J. Mar. Res.* **56**, 1029–1067 (1998).

63. V. V. S. S. Sarma, An evaluation of physical and biogeochemical processes regulating perennial suboxic conditions in the water column of the Arabian Sea. *Global Biogeochem. Cycles* **16**, 29–1–29–11 (2002).

64. T. J. Heaton, P. Köhler, M. Butzin, E. Bard, R. W. Reimer, W. E. N. Austin, C. Bronk Ramsey, P. M. Grootes, K. A. Hughen, B. Kromer, P. J. Reimer, J. Adkins, A. Burke, M. S. Cook, J. Olsen, L. C. Skinner, Marine20—The marine radiocarbon age calibration curve (0–55,000 cal BP). *Radiocarbon* **62**, 779–820 (2020).

65. J. Southon, M. Kashgarian, M. Fontugne, B. Metivier, W. W.-S. Yim, Marine reservoir corrections for the Indian ocean and southeast Asia. *Radiocarbon* **44**, 167–180 (2002).

66. M. Blaauw, J. A. Christeny, Flexible paleoclimate age-depth models using an autoregressive gamma process. *Bayesian Anal.* **6**, 457–474 (2011).

67. C. M. Ostrander, J. D. Owens, S. G. Nielsen, Constraining the rate of oceanic deoxygenation leading up to a Cretaceous Oceanic Anoxic Event (OAE-2: ~94 Ma). *Sci. Adv.* **3**, e1701020 (2017).

68. S. G. Nielsen, M. Rehkämper, J. Baker, A. N. Halliday, The precise and accurate determination of thallium isotope compositions and concentrations for water samples by MC-ICPMS. *Chem. Geol.* **204**, 109–124 (2004).

69. M. Rehkämper, M. Frank, J. R. Hein, D. Porcelli, A. Halliday, J. Ingri, V. Liebetrau, Thallium isotope variations in seawater and hydrogenetic, diagenetic, and hydrothermal ferromanganese deposits. *Earth Planet. Sci. Lett.* **197**, 65–81 (2002).

70. Y. Shu, S. G. Nielsen, Z. Zeng, R. Shinjo, J. Blusztajn, X. Wang, S. Chen, Tracing subducted sediment inputs to the Ryukyu arc-Okinawa Trough system: Evidence from thallium isotopes. *Geochim. Cosmochim. Acta* **217**, 462–491 (2017).

71. J. Ahrens, M. Beck, P. Böning, J. Degenhardt, K. Pahnke, B. Schnetger, H. J. Brumsack, Thallium cycling in pore waters of intertidal beach sediments. *Geochim. Cosmochim. Acta* **306**, 321–339 (2021).

72. R. L. Rudnick, S. Gao, "Composition of the continental crust" in *Treatise on Geochemistry*, vol. 3, H. D. Holland, K. K. Turekian, Eds. (Pergamon, 2003), pp. 1–64.

73. S. G. Nielsen, M. Goff, S. P. Hesselbo, H. C. Jenkyns, D. E. LaRowe, C.-T. A. Lee, Thallium isotopes in early diagenetic pyrite – A paleoredox proxy? *Geochim. Cosmochim. Acta* **75**, 6690–6704 (2011).

74. R. E. Chandler, E. M. Scott, *Statistical Methods for Trend Detection and Analysis in the Environmental Sciences* (John Wiley & Sons, 2011).

75. R. Schlitzer, Ocean Data View (2018); https://odv.awi.de.

76. Z. Erdem, J. Schönfeld, A. E. Rathburn, M. E. Pérez, J. Cardich, N. Glock, Bottom-water deoxygenation at the Peruvian margin during the last deglaciation recorded by benthic foraminifera. *Biogeosciences* **17**, 3165–3182 (2020).

77. F. Marcantonio, R. Hostak, J. E. Hertzberg, M. W. Schmidt, Deep equatorial Pacific ocean oxygenation and atmospheric CO$_2$ over the last ice age. *Sci. Rep.* **10**, 6606 (2020).

78. Z. Lu, B. A. A. Hoogakker, C.-D. Hillenbrand, X. Zhou, E. Thomas, K. M. Gutchess, W. Lu, L. Jones, R. E. M. Rickaby, Oxygen depletion recorded in upper waters of the glacial Southern Ocean. *Nat. Commun.* **7**, 11146 (2016).

79. S. E. Moffitt, T. M. Hill, P. D. Roopnarine, J. P. Kennett, Response of seafloor ecosystems to abrupt global climate change. *Proc. Natl. Acad. Sci. U. S. A.* **112**, 4684–4689 (2015).

80. A. Durand, Z. Chase, T. L. Noble, H. Bostock, S. L. Jaccard, A. T. Townsend, N. L. Bindoff, H. Neil, G. Jacobsen, Reduced oxygenation at intermediate depths of the southwest Pacific during the last glacial maximum. *Earth Planet. Sci. Lett.* **491**, 48–57 (2018).

81. M. Luo, T. J. Algeo, H. Tong, J. Gieskes, L. Chen, X. Shi, D. Chen, More reducing bottom-water redox conditions during the last glacial maximum in the southern challenger deep (Mariana trench, western pacific) driven by enhanced productivity. *Deep Sea Res. Part II Top. Stud. Oceanogr. DEEP-SEA RES PT II* **155**, 70–82 (2018).

82. J. Zou, X. Shi, A. Zhu, S. Kandasamy, X. Gong, L. Lembke-Jene, M. te Chen, Y. Wu, S. Ge, Y. Liu, X. Xue, G. Lohmann, R. Tiedemann, Millennial-scale variations in sedimentary oxygenation in the western subtropical North Pacific and its links to North Atlantic climate. *Clim. Past* **16**, 387–407 (2020).

83. E. Ovsepyan, E. Ivanova, M. Tetard, L. Max, R. Tiedemann, Intermediate- and deep-water oxygenation history in the subarctic north pacific during the last deglacial period. *Front. Earth Sci.* **9**, 718 (2021).

84. G. Li, H. Rashid, L. Zhong, X. Xu, W. Yan, Z. Chen, Changes in deep water oxygenation of the south China sea since the last glacial period. *Geophys. Res. Lett.* **45**, 9058–9066 (2018).

85. Sharon, C. S. Belanger, J. Du, A. Mix, Reconstructing paleo-oxygenation for the last 54,000 years in the gulf of Alaska using cross-validated benthic foraminiferal and geochemical records. *Paleoceanogr. Paleoclimatol.* **36**, e2020PA003986 (2021).

86. Y. Dou, S. Yang, C. Li, X. Shi, J. Liu, L. Bi, Deepwater redox changes in the southern Okinawa Trough since the last glacial maximum. *Prog. Oceanogr.* **135**, 77–90 (2015).

87. D. Gallego-Torres, O. E. Romero, F. Martínez-Ruiz, J. H. Kim, B. Donner, M. Ortega-Huertas, Rapid bottom-water circulation changes during the last glacial cycle in the coastal low-latitude NE Atlantic. *Quatern. Res.* **81**, 330–338 (2014).

88. M. Tetard, L. Licari, L. Beaufort, Oxygen history off Baja California over the last 80 kyr: A new foraminiferal-based record. *Paleoceanography* **32**, 246–264 (2017).

89. W. Lu, C. F. Barbosa, A. E. Rathburn, P. d. M. Xavier, A. P. S. Cruz, E. Thomas, R. E. M. Rickaby, Y. G. Zhang, Z. Lu, Proxies for paleo-oxygenation: A downcore comparison between benthic foraminiferal surface porosity and I/Ca. *Palaeogeogr. Palaeoclimatol. Palaeoecol.* **579**, 110588 (2021).

90. M. Wagner, I. L. Hendy, Trace metal evidence for a poorly ventilated glacial Southern Ocean. *Quat Sci Rev* **170**, 109–120 (2017).

91. B. Gaye, A. Böll, J. Segschneider, N. Burdanowitz, K. C. Emeis, V. Ramaswamy, N. Lahajnar, A. Lückge, T. Rixen, Glacial-interglacial changes and Holocene variations in Arabian Sea denitrification. *Biogeosciences* **15**, 507–527 (2018).

92. J. Gottschalk, L. C. Skinner, J. Lippold, H. Vogel, N. Frank, S. L. Jaccard, C. Waelbroeck, Biological and physical controls in the Southern Ocean on past millennial-scale atmospheric CO$_2$ changes. *Nat. Commun.* **7**, 11539 (2016).

93. A. van Geen, Y. Zheng, J. M. Bernhard, K. G. Cannariato, J. Carriquiry, W. E. Dean, B. W. Eakins, J. D. Ortiz, J. Pike, On the preservation of laminated sediments along the western margin of North America. *Paleoceanography* **18**, 1098 (2003).

94. B. K. S. Gupta, M. L. Machain-Castillo, Benthic foraminifera in oxygen-poor habitats. *Mar. Micropaleontol.* **20**, 183–201 (1993).

95. M. Tetard, L. Licari, E. Ovsepyan, K. Tachikawa, L. Beaufort, Toward a global calibration for quantifying past oxygenation in oxygen minimum zones using benthic Foraminifera. *Biogeosciences* **18**, 2827–2841 (2021).

96. M. A. Altabet, C. Pilskaln, R. Thunell, C. Pride, D. Sigman, F. Chavez, R. Francois, The nitrogen isotope biogeochemistry of sinking particles from the margin of the Eastern North Pacific. *Deep Sea Res. Part I Oceanogr. Res. Pap.* **46**, 655–679 (1999).

97. S. E. Calvert, T. F. Pedersen, "Elemental proxies for Palaeoclimatic and Palaeoceanographic variability in marine sediments: Interpretation and application" in *Developments in Marine Geology*, vol. 1 (2007), pp. 567–644.

98. R. F. Anderson, J. P. Sachs, M. Q. Fleisher, K. A. Allen, J. Yu, A. Koutavas, S. L. Jaccard, Deep-sea oxygen depletion and ocean carbon sequestration during the last ice age. *Global Biogeochem. Cycles* **33**, 301–317 (2019).

99. Z. Lu, H. C. Jenkyns, R. E. M. Rickaby, Iodine to calcium ratios in marine carbonate as a paleo-redox proxy during oceanic anoxic events. *Geology* **38**, 1107–1110 (2010).

100. A. E. Rathburn, J. Willingham, W. Ziebis, A. M. Burkett, B. H. Corliss, A New biological proxy for deep-sea paleo-oxygen: Pores of epifaunal benthic foraminifera. *Sci. Rep.* **8**, 9456 (2018).

101. J. D. Owens, *Application of Thallium Isotopes: Tracking Marine Oxygenation through Manganese Oxide Burial* (Cambridge Univ. Press, 2019).

102. K. S. Johnson, K. H. Coale, W. M. Berelson, R. M. Gordon, On the formation of the manganese maximum in the oxygen minimum. *Geochim. Cosmochim. Acta* **60**, 1291–1299 (1996).

103. E. L. Rue, G. J. Smith, G. A. Cutter, K. W. Bruland, The response of trace element redox couples to suboxic conditions in the water column. *Deep Sea Res. Part I Oceanogr. Res.* **44**, 113–134 (1997).

104. S. J. Schenau, G. J. Reichart, G. J. de Lange, Oxygen minimum zone controlled Mn redistribution in Arabian Sea sediments during the late Quaternary. *Paleoceanography* **17**, 10–1–10–12 (2002).

105. D. Kadko, A. Aguilar-Islas, C. Bolt, C. S. Buck, J. N. Fitzsimmons, L. T. Jensen, W. M. Landing, C. M. Marsay, R. Rember, A. M. Shiller, L. M. Whitmore, R. F. Anderson, The residence times of trace elements determined in the surface Arctic Ocean during the 2015 US Arctic GEOTRACES expedition. *Mar. Chem.* **208**, 56–69 (2019).

106. J. Crusius, T. F. Pedersen, S. Kienast, L. Keigwin, L. Labeyrie, Influence of northwest pacific productivity on north Pacific intermediate water oxygen concentrations during the Bølling-Ållerød interval (14.7–12.9 ka). *Geology* **32**, 633–636 (2004).

107. I. L. Hendy, T. F. Pedersen, Oxygen minimum zone expansion in the eastern tropical North Pacific during deglaciation. *Geophys. Res. Lett.* **33**, 20 (2006).

108. B. M. Tebo, Manganese(II) oxidation in the suboxic zone of the Black Sea. *Deep Sea Res. A* **38**, S883–S905 (1991).

109. D. C. Lund, P. D. Asimow, K. A. Farley, T. O. Rooney, E. Seeley, E. W. Jackson, Z. M. Durham, Enhanced East Pacific Rise hydrothermal activity during the last two glacial terminations. *Science* **351**, 478–482 (2016).

110. J. B. Corliss, J. Lyle, J. Dymond, K. Crane, The chemistry of hydrothermal mounds near the Galapagos Rift. *Earth Planet. Sci. Lett.* **40**, 12–24 (1978).

111. J. Gottschalk, E. Michel, L. M. Thöle, A. S. Studer, A. P. Hasenfratz, N. Schmid, M. Butzin, A. Mazaud, A. Martínez-García, S. Szidat, S. L. Jaccard, Glacial heterogeneity in Southern Ocean carbon storage abated by fast South Indian deglacial carbon release. *Nat. Commun.* **11**, 6192 (2020).

112. N. Lathika, W. Rahaman, M. Tarique, N. Gandhi, A. Kumar, M. Thamban, Deep water circulation in the Arabian Sea during the last glacial cycle: Implications for paleo-redox condition, carbon sink and atmospheric CO_2 variability. *Quat. Sci. Rev.* **257**, 106853 (2021).

113. F. Lambert, M. Bigler, J. P. Steffensen, M. Hutterli, H. Fischer, Centennial mineral dust variability in high-resolution ice core data from Dome C, Antarctica. *Clim. Past* **8**, 609–623 (2012).

114. S. G. Nielsen, M. Rehkämper, D. Porcelli, P. Andersson, A. N. Halliday, P. W. Swarzenski, C. Latkoczy, D. Günther, Thallium isotope composition of the upper continental crust and rivers—An investigation of the continental sources of dissolved marine thallium. *Geochim. Cosmochim. Acta* **69**, 2007–2019 (2005).

115. M. Rehkämper, S. G. Nielsen, The mass balance of dissolved thallium in the oceans. *Mar. Chem.* **85**, 125–139 (2004).

116. S. G. Nielsen, M. Rehkämper, D. A. H. Teagle, D. A. Butterfield, J. C. Alt, A. N. Halliday, Hydrothermal fluid fluxes calculated from the isotopic mass balance of thallium in the ocean crust. *Earth Planet. Sci. Lett.* **251**, 120–133 (2006).

117. R. G. A. Baker, M. Rehkämper, T. K. Hinkley, S. G. Nielsen, J. P. Toutain, Investigation of thallium fluxes from subaerial volcanism—Implications for the present and past mass balance of thallium in the oceans. *Geochim. Cosmochim. Acta* **73**, 6340–6359 (2009).

ScienceAdvances

Global oceanic oxygenation controlled by the Southern Ocean through the last deglaciation

Yi Wang, Kassandra M. Costa, Wanyi Lu, Sophia K. V. Hines, and Sune G. Nielsen

View the article online
https://www.science.org/doi/10.1126/sciadv.adk2506
Permissions
https://www.science.org/help/reprints-and-permissions